Design of Superior Spider Silk: From Nanostructure to Mechanical Properties

Ning Du,* Xiang Yang Liu,* Janaky Narayanan,* Lian Li,* Matthew Lek Min Lim,† and Daiqin Li†
*Department of Physics and †Department of Biological Science, National University of Singapore, Singapore

ABSTRACT Spider dragline silk is of practical interest because of its excellent mechanical properties. However, the structure of this material is still largely unknown. In this article, we report what we believe is a new model of the hierarchical structure of silk based on scanning electron microscope and atomic force microscope images. This hierarchical structure includes β-sheet, polypeptide chain network, and silk fibril. It turns out that an exceptionally high strength of the spider dragline silk can be obtained by decreasing the size of the crystalline nodes in the polypeptide chain network while increasing the degree of orientation of the crystalline nodes. Based on this understanding, how the reeling speed affects mechanical properties of spider dragline silk can be understood properly. Hopefully, the understanding obtained in this study will shed light on the formation of spider silk, and consequently, on the principles for the design of ultrastrong silk.

INTRODUCTION

Spider silk fibers are of practical interest because of their excellent mechanical property (1–4). They are strong and tough, designed by nature in an optimal way to fulfill a wide range of functions using subtle changes in chemical composition and, more importantly, morphological structure at a nanometer scale (5). Spider dragline silk is a high-performance fiber with mechanical properties rivaling the best man-made materials (6). It is a composite material with a hierarchical structure, composed mainly of two proteins, Spidroin I and II (7). The molecular structure that leads to the functional properties of the material, however, is far from being understood.

There is increasing evidence that the structure higher up in the hierarchy is not solely determined by the primary structure: beyond the secondary structure includes tertiary structure as well as the nanocrystals and a nanofibrillar organization of the silk thread (8). The poly-Ala domains in Spidroin I have previously been characterized by NMR and x-ray diffraction. They were found to be predominantly in β-sheet conformation (9) and to organize into crystallites (10). The crystalline portion of the fibroins consists of antiparallel pleated sheets of polypeptide chains packed into an orthorhombic unit cell (11). These crystallites are interconnected in an amorphous glycine-rich matrix (12). It is apparent that the intramolecular as well as intermolecular organization of the proteins of the dragline silk thread are critical for spider silk performance (13). The spinning process itself has an important influence on silk structure and the mechanical properties of the silk (14). It has been found the mechanical properties of the *Nephila* spider dragline silk vary considerably with the speed of drawing (5,15). It is our purpose in this research to examine the mechanical and structural characterization of spider dragline silk at various reeling speeds to establish the relationship between the nanostructure and mechanical properties of spider silk. Based on the structural feature of spider dragline silk obtained from x-ray scattering and atomic force microscope (AFM) measurements, a model is set up to describe the structure of spider dragline silk at the nanoscale and demonstrate the effect of the reeling speed on the structure and mechanical properties of spider silk. This understanding will allow us to identify a robust technique to fabricate ultraperformance silks.

MATERIALS AND METHODS

Silk sampling

Adult females of spider *Nephila pilipes* were slightly anaesthetized by CO_2 and fixed with soft tape to a metal block. We waited at least 30 min to minimize any residual effects of the anesthesia (16). A computer-controlled motorized spindle allowed drawing fibers in a wide range of well-defined speeds. The abdominal temperature of the spider was held constant at the ambient room temperature of 22°C.

SEM and AFM imaging

AFM imaging was performed by standard procedures in taping mode by Nanoscope III (Veeco, Woodbury, NY) scanning force microscope. Scanning electron microscope (SEM) measurements were carried out on a JEOL (Tokyo, Japan) JSM6700F.

X-ray scattering

The wide angle x-ray scattering (WAXS) patterns of a bundle of 800 spider dragline silk filaments were collected using Bruker GADDS XRD with beam size 0.5 mm. The radiation wavelength is 1.5418 Å for Cu Kα. The sample-to-detector distance was 6 cm and the exposure time was 30 min. The small angle x-ray scattering (SAXS) experiments were performed with a Bruker NanoSTAR small angle x-ray scattering system. The generator was

Submitted May 16, 2006, and accepted for publication August 21, 2006.

Address reprint requests to Xiang Yang Liu, Dept. of Physics, National University of Singapore, 2 Science Drive 3, Singapore 117542. Tel.: 65-651-62812; Fax: 65-677-76126; Email: phyliuxy@nus.edu.sg.

0006-3495/06/12/4528/08 $2.00

doi: 10.1529/biophysj.106.089144

operated at 40 kV and 35 mA. A double pinhole system creates an x-ray spot with diameter 200 μm on the silk and the detector has a spatial resolution of 10 μm. The detector-to-sample distance is 107 cm. The sample chamber was vacuumed to eliminate the scattering of air. The silk filaments were put in parallel with each other between two thin glass plates of thickness 0.1 mm, which were glued together on the edges to prevent water evaporation from the silk in vacuum.

Mechanical tests

An Instron MicroTester was used to measure the force-extension characteristics of the silk. A thread was fixed between two hooks of the instrument, which had a gauge length of 20 mm with a measured error of 0.1 mm. The thread was stretched until it broke and the stain rate was 50% per minute. The experiments were operated at 22°C and humidity was kept at 81%.

RESULTS AND DISCUSSION

Topological imaging

The silk fibril structure of spider dragline silk was observed by SEM and AFM (Fig. 1, *a* and *b*). The silk thread, having a diameter of 4–5 μm, consists of a number of silk fibrils with diameter 40–80 nm. Similar silk fibril images are found in other references (17,18). It is not surprising to find that the silk is composed of so many silk fibrils along the silk thread axis, considering the structure of the spider spinneret with hundreds of tubes coming from the silk glands (19). According to AFM images, a silk fibril is not a cylindrical fibril but some of its segments are interlinked with each other. As the imaging of AFM is based on the force profile, segments represent the regions that may have harder materials, such as protein polypeptide networks that are interlinked by rather soft or flexible polypeptide chains.

Based on these images, a model is proposed for describing the hierarchical structure of spider dragline silk as illustrated in Fig. 1. Several β-sheets (crystalline domains) connected by non-β-structure (noncrystalline domains) form one silk fibril segment (as indicated by the *dashed circle* in Fig. 1, *b* and *c*). Many of these silk fibril segments are interlinked with each other, so as to compose one single silk fibril along the silk thread axis. The size and orientation of the crystallites as well as the intercrystallite distance within the silk fibril can be determined by x-ray diffraction (see following sections for details). This allows us to establish the correlation between the structure and the mechanical properties of the silk obtained at different reeling speeds.

Crystallite size

Radial integration along the equator and meridian on the WAXS pattern gives the radial peak width on the (200), (120), and (002) reflections. According to Scherrer's formula (20), the crystal size is

$$L = \frac{0.9\lambda}{\mathrm{FWHM}\cos\theta}, \quad (1)$$

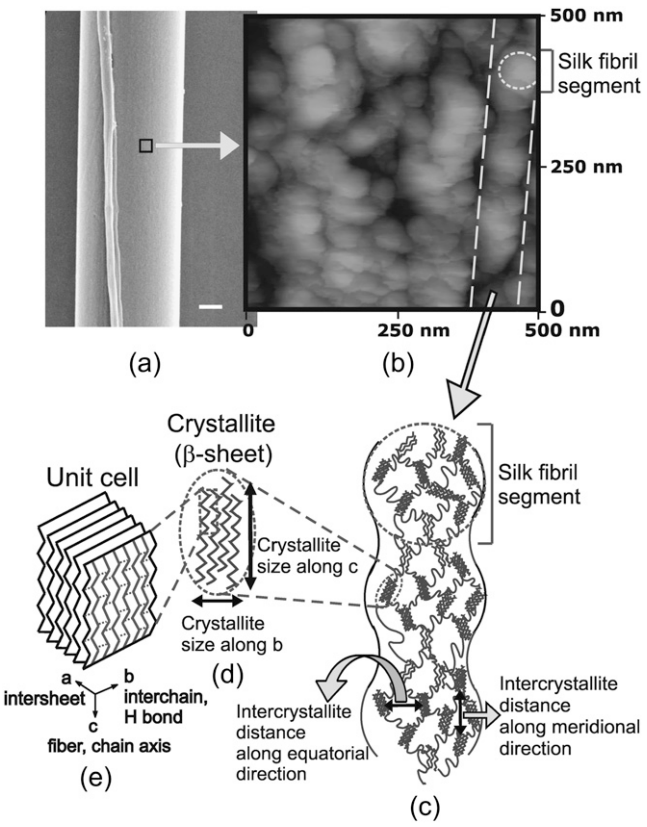

FIGURE 1 Hierarchical structure of spider dragline silk *N. pilipes*. (*a*) SEM image of spider dragline silk. Scale bar, 1 μm. (*b*) AFM image showing the silk fibril structure as the dashed lines indicate. Each silk fibril is composed of interconnected ''silk fibril segments'' as indicated by the dashed circle of size 40–80 nm. (*c*) Proposed model for the silk fibril structure: the ''silk fibril segment'' consists of several β-sheets connected by random coil or α-helix forming a protein polypeptide chain network. The mesh size of the network is the intercrystallite distance. (*d*) The crystallites in silk fibril have a β-sheet structure. The crystallite size and orientation can be determined by x-ray diffraction. (*e*) Unit cell of silk crystallite has an antiparallel β-sheet configuration. (Dashed lines indicate the hydrogen bonds between protein chains within one β-sheet.)

where FWHM is full width at half-maximum of the peak at the diffraction angle of θ and $\lambda = 1.5418$ Å (Cu Kα). The equatorial data were deconvoluted into three crystalline peaks corresponding to (100), (200), and (120) Bragg reflections and an amorphous halo (21) (Fig. 2). Similarly, the meridian data show a crystalline peak corresponding to the (002) reflection and a broad amorphous halo. The position and FWHM of these peaks were used to determine the crystallite size along the $\vec{a}$, $\vec{b}$, and $\vec{c}$ axes. As shown in Table 1, the crystallites become smaller or the crystalline order becomes poorer with reeling speed.

The effect of reeling speed on the crystallite size can be explained by the nucleation kinetics. The formation of β-sheet crystallites is controlled by nucleation and growth processes (22). Some portion of the protein chains undergoes nucleation when extruded from the spinneret orifice and

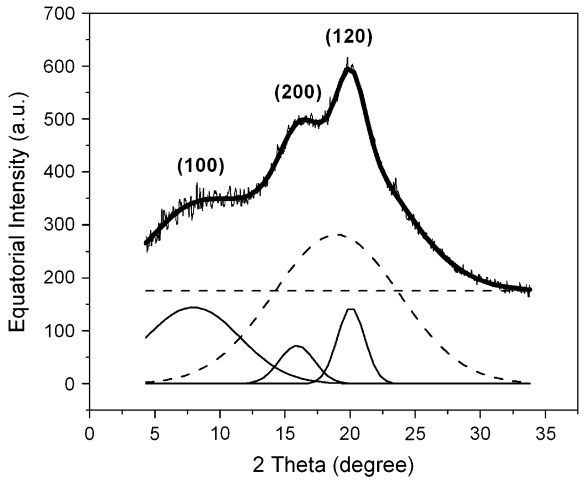

FIGURE 2 Intensity as a function of scattering angle 2θ at 10 mms^{-1} along equatorial direction. The peaks are fitted as the sum of four Gaussians: three crystalline peaks and one amorphous halo. The three crystalline peaks are indexed as (100), (200), and (120), according to Warwicker (11).

crystallizes as the solvent evaporates. The study of the silk secretion of *Bombyx mori* and *Nephila clavipes* when the silk secretion is put on a glass slide indicates that a liquid crystalline phase occurs quickly followed by a slow formation of the crystalline phase (23). This suggests that the amorphous-to-crystalline phase transition much depends on the initial concentration and subsequent drying rate, i.e., supersaturation of the silk protein solution. Before the silk is extruded, it passes through a long thin duct (24). The shearing of the fluid in the duct compels the protein chains to extend in the direction of the flow, and compels them to come closer to each other. This process increases the concentration (supersaturation) of the protein chain. When the silk is extruded at the spinneret orifice, the supersaturation increases rapidly with evaporation. This induces the nucleation between protein chains. Nucleation is the process with which phase transitions begin. The driving force for the nucleation of new phases (e.g., crystals) is $\Delta\mu$, which is defined as the difference between the chemical potentials μ_{mother} and μ_{crystal} of the growth unit in the mother and the crystalline phases. Expressing $\Delta\mu$ in terms of the supersaturation σ, we have (25)

$$\Delta\mu = kT\ln(1+\sigma), \tag{2}$$

where $\sigma = (C_i - C_i^{eq})/C_i^{eq}$, and C_i and C_i^{eq} denote the concentrations of the solute and the equilibrium concentrations of solute, respectively. The radius of the critical nuclei is determined by the driving force $\Delta\mu$ (25)

$$r_c \propto \frac{1}{\Delta\mu} = \frac{1}{kT\ln(1+\sigma)}. \tag{3}$$

At higher reeling speed, the silk extruded at the spinneret evaporates faster, thus σ is large. According to Eq. 3, the crystallite size is in inverse proportion to $\ln(1+\sigma)$. Therefore, the crystallites become smaller at a higher reeling speed.

In addition, we can get a relation between the supersaturation σ and nucleation rate J,

$$J \propto \exp\left(-\frac{p}{[\ln(1+\sigma)]^2}\right), \tag{4}$$

where the nucleation rate J is defined as the number of nuclei created per unit volume time and p is a system-dependent parameter. According to Eq. 4, when the silk is drawn faster, the nucleus density within the silk will rise as the supersaturation σ is high at a higher reeling speed.

It was reported that the crystallinity (the percentage of crystalline phase) of silk is proportional to the rate of drawing (26). This implies that although the crystallites are smaller at higher reeling speeds, the whole crystalline proportion increases due to the increase in the crystallite density with increasing reeling speed.

TABLE 1 Crystallite size along $\vec{a}$, $\vec{b}$, $\vec{c}$ directions for different reeling speeds, as obtained from the width and position of the (200), (120), and (002) peaks using the Scherrer equation

	Crystallite size (nm)		
Reeling speed (mms^{-1})	$\vec{a}$	$\vec{b}$	$\vec{c}$
1	2.4	3.5	7.3
2.5	2.3	3.4	7.1
10	2.1	2.7	6.5
25	2.2	2.7	6.4
100	2.1	2.7	6.4

Orientation distribution

We can obtain the orientation of the crystallites about the thread axis from the intensity integration as a function of azimuth angle at the radial position of equatorial (120) and (200) peaks (Fig. 3). The widths of the azimuth angular distribution for different reeling speeds are listed in Table 2. The Hermans orientation function $f = (3\langle\cos^2\phi\rangle - 1)/2$, where ϕ is the angle between the $\vec{c}$ axis and the fiber axis. The parameter f is 0 for no preferred orientation in fibers and 1 if all crystals are perfectly aligned with respect to each other. For two reflections, (200) and (120), which are not orthogonal but have a known geometry in the equatorial plane, we have

$$\langle\cos^2\phi\rangle = 1 - A\langle\cos^2\phi_1\rangle - B\langle\cos^2\phi_2\rangle. \tag{5}$$

Since (120) is 65° from the (200), $A = 0.8$ and $B = 1.2$. The data in Table 2 are measured perpendicular to the fiber axis, so $\varphi = 90° - \phi$, thus $\langle\cos^2\phi\rangle = 1 - \langle\cos^2\varphi\rangle$. For a Gaussian, $\langle\cos^2\varphi\rangle = \{\cos(0.4FWHM)\}^2$. The data in Table 2 can thus be used to find the orientation function f.

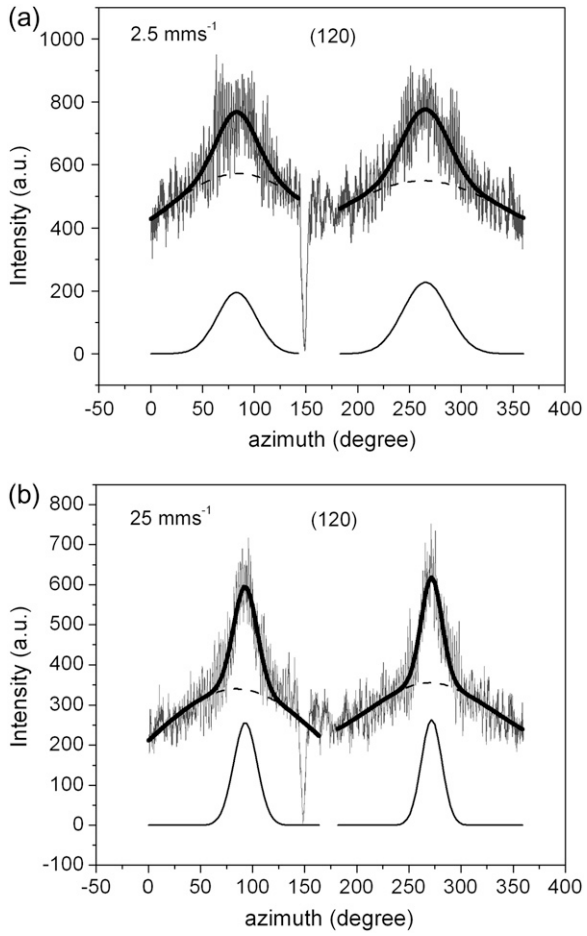

FIGURE 3 Intensity as a function of azimuth angle at the radial position of the equatorial (120) peak: (*a*) at 2.5 mms^{-1} and (*b*) at 25 mms^{-1}. The peaks are fitted as sums of two Gaussians, corresponding to crystalline (narrow) and amorphous (broad) distributions.

As shown in Table 2, both (120) and (200) peaks become narrower as the reeling speed increases. These data imply that the orientation function undergoes a tremendous increase with the reeling speed, from 0.68 for 1 mms^{-1} to 0.97 for 100 mms^{-1}(Fig. 4). This means that a high reeling speed can induce a better orientation along the thread axis, which is consistent with the other observations (27).

TABLE 2 Width of azimuth angular distribution with reeling speed for (200) and (120) peaks

Reeling speed (mms^{-1})	FWHM for (200) peak	FWHM for (120) peak
1	42.1 ± 3.2	49.9 ± 2.8
2.5	37.0 ± 2.7	46.3 ± 3.0
10	24.5 ± 1.3	20.1 ± 0.8
25	21.1 ± 0.8	17.6 ± 0.4
100	15.2 ± 0.5	14.3 ± 0.3

The widths are given as FWHM in degrees.

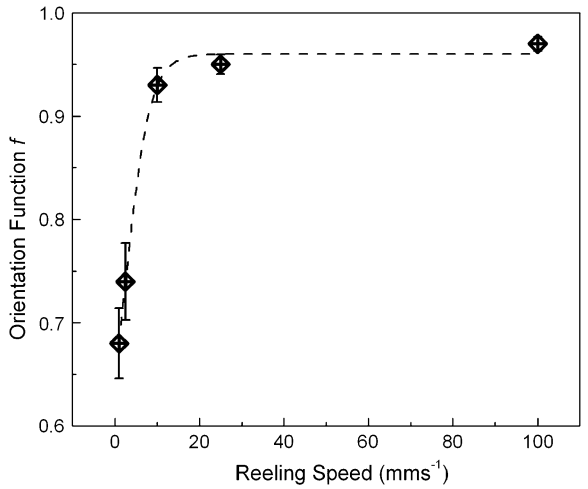

FIGURE 4 Orientation function *f*, calculated from FWHM, increases with reeling speed.

Intercrystallite distance

Assuming that the scatter are the crystallites embedded in the amorphous silk region, and that they have cylindrical symmetry along the fiber axis, the SAXS intensity in the equatorial direction can be given as (28)

$$I = \frac{Kl_c^2}{(1 + l_c^2 q^2)^{3/2}}, \tag{6}$$

where $q = 4\pi\sin\theta/\lambda$ is the scattering wave vector. Here θ is the scattering angle and λ is the x-ray wavelength. l_c is the correlation length, and it can be determined from the intercept and slope of a plot of $I^{-2/3}$ versus q^2. For the scattering along the meridional direction, Eq. 6 takes a slightly different form:

$$I = \frac{Kl_c^2}{1 + l_c^2 q^2}. \tag{7}$$

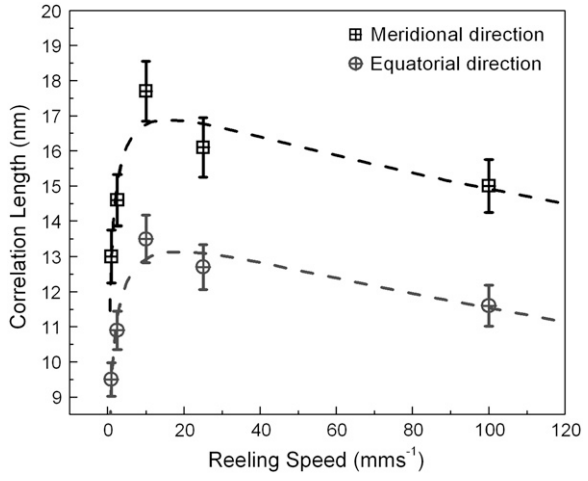

FIGURE 5 Correlation length in spider silk along the meridional and equatorial directions measured from SAXS.

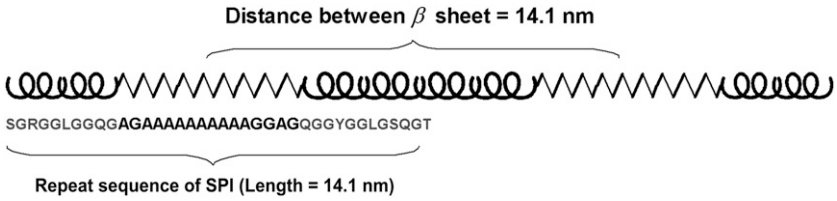

FIGURE 6 Repeat sequence and secondary structure of SPI. The distance between β-sheets is equal to the length of SPI (= 14.1 nm).

The correlation length l_c along the meridian is determined from the intercept and slope of the plot of I^{-1} versus q^2. The correlation lengths calculated for different reeling speeds using Eqs. 6 and 7 are shown in Fig. 5. The correlation lengths can be related to intercrystallite distance. A similar analysis is used in the SAXS study of the semicrystalline fibers (29) and the small angle neutron scattering study of poly(vinyl alcohol) gels in which the cross-linking points are crystallites (30). However, unlike the gels, the silk has a fiber axis with different material properties along the equatorial and meridional directions. Hence the correlation lengths are considered separately along these directions.

Two consensus sequences, Spidroin I and Spidroin II, represent major repetitive elements from spider dragline silk. The Spidroin I (SPI) repeat sequence consists of 38 aa and includes 16-aa-long poly(A) and poly(GA) stretches, flanked on both sides with a total of 22 aa forming glycine-rich GGX motifs (13). The poly(A) and poly(GA) domains are predominantly in β-sheet conformation and organized into crystals. These β-sheets alternate sequences of the SPI molecules, which form random coils or non-α-helices (13). From the SPI sequence, the distance between the β-sheets is 14.1 nm (Fig. 6). This value agrees with the correlation length along the meridional direction (fiber axis) measured from SAXS, which is ~13–18 nm (Fig. 5).

From Fig. 5, we find that when the silk is entrained faster, the distance between the crystallites (correlation length) becomes larger along both the meridional and equatorial directions up to a reeling speed of ~10 mms^{-1}. This is because the amorphous chains are in a relaxed state and loosely packed at low reeling speed. When the silk is stretched at high speed, the chains are easily extended in the direction of fiber axis under high shearing force. Consequently, the intercrystallite distance becomes larger. When the silk is stretched at still higher reeling speed (>10 mms^{-1}), the silk fibril segments start merging together while the diameter of the silk thread drops (15) and hollow regions begin to appear. Hence the distance between the crystallites decreases. The

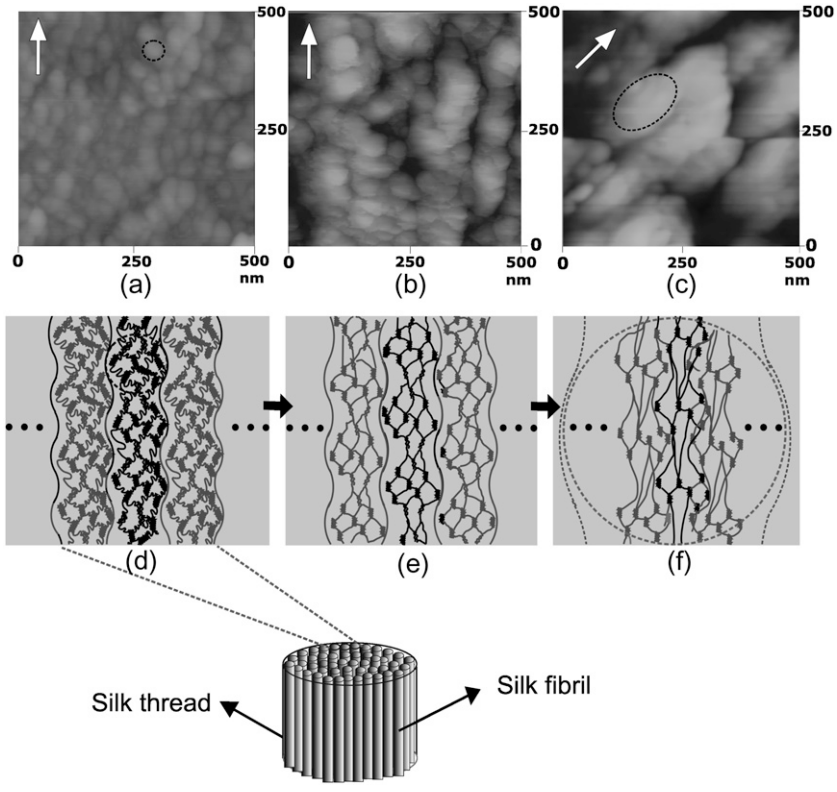

FIGURE 7 Topographic AFM image of spider dragline silk *N. pilipes* at different reeling speeds and the proposed model for the corresponding structure change with increasing reeling speed: (*a*) at 2.5 mms^{-1}, (*b*) at 25 mms^{-1}, and (*c*) at 100 mms^{-1}. The direction of thread is indicated by the arrow. (*d*) At low reeling speed (<2 mms^{-1}), crystallites are less well-oriented and the amorphous chains are relaxed. (*e*) With increasing reeling speed, the crystallites are smaller and better oriented. At the same time, the intercrystallite distance becomes larger. (*f*) Further increase of the reeling speed (>10 mms^{-1}) causes nanofibrils to merge further together, and the observed ''particle size'' as indicated by a dashed circle becomes larger, thus the distance between the crystallites becomes smaller.

merging of the silk fibril segments was observed with AFM (Fig. 7, *a–c*). Comparison of Fig. 7 *a* with Fig. 7, *b* and *c*, clearly shows the difference of ''particle size'' due to the mergence of the silk fibril segments at higher reeling speed. A model for describing the corresponding nanostructure change with increasing reeling speed is illustrated in Fig. 7, *d–f*. An alternative explanation for the decrease of the intercrystallite distance above 10 mms^{-1} may be obtained from the relation between the nucleation rate and reeling speed. According to Eq. 4, the crystallite density within the silk rises with the increasing reeling speed. Accordingly, the intercrystallite distance becomes shorter as the reeling speed increases.

The above results on the size measurement of silk fibril segments using AFM (40–80 nm), together with the results of the crystallite size (2–7 nm) and intercrystallite distance (13–18 nm) measured with x-ray diffraction confirm the correctness of the relationship between crystallite and silk fibril segments proposed in Fig. 1, i.e., that each silk fibril segment consists of several crystallites connected by non-β-structures. This feature of the nanostructure of spider dragline silk may play an important role in contributing to its high mechanical performance.

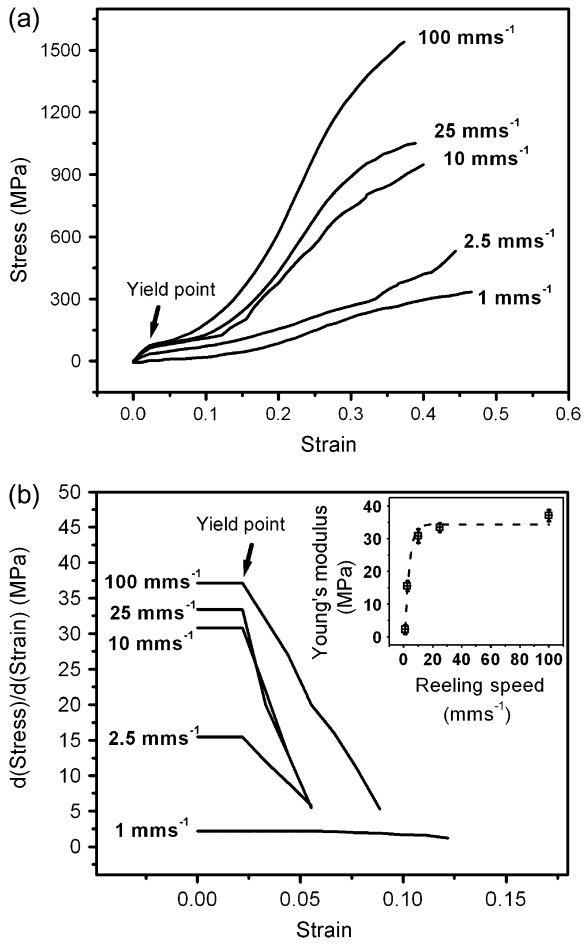

FIGURE 8 Comparison of silks drawn at different speeds from spider *N. pilipes*. (*a*) Stress-strain curve. The curves start to deviate from the first linear part at the yield point. The stress and strain at the yield point are called ''yield stress'' and ''yield strain''. respectively. (*b*) The slope of the stress-strain curve in *a* versus strain at low strain showing the yield point. (*Inset*) The calculated Young's modulus (slope in the linear region of the stress-strain curve) with reeling speed.

The relation between the nanostructure and mechanical property

The mechanical properties of spider dragline silk vary considerably with the reeling speed (Fig. 8). The stress-strain curves start to deviate from the first linear part at the yield point. The stress and strain at the yield point are called ''yield stress'' and ''yield strain'', respectively, and the slope of the stress-strain curve between the origin and the yield point is Young's modulus (31). These parameters can be calculated from stress-strain curve and the results are shown in Figs. 8 *b* and 9. The physical properties of silk should be determined at the molecular level by a number of structural factors, such as crystallite size and orientation, and

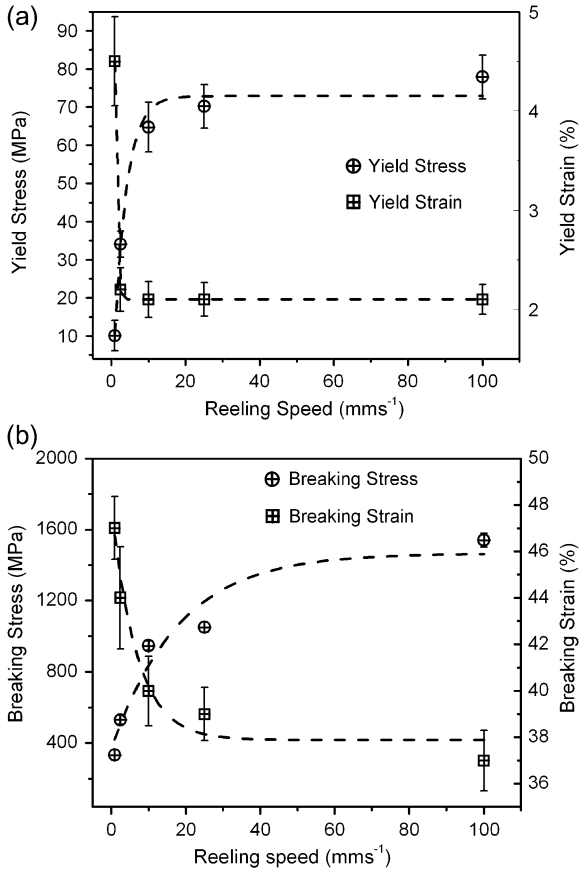

FIGURE 9 Effect of the reeling speed on the mechanical property of spider dragline silk. (*a*) The effect on stress. (*b*) The effect on strain.

intercrystallite distance. It appears from the results presented in Fig. 4 that until the natural reeling speed for spiders (10–20 mms^{-1}, from Shao et al.(32)) is reached, the orientation of the crystallites reaches an equilibrium value (orientation function $f = 0.94$). It is interesting to find that Young's modulus and the yield stress attain their maximum values at the same reeling speed (increased ~10 times for Young's modulus and 7 times for yield stress at 10–20 mms^{-1} compared with those at 1 mms^{-1}). This may imply a direct relationship between crystallite orientation and Young's modulus/yield stress. As shown in Fig. 10, the yield stress appears to increase substantially linearly with increasing orientation. Moreover, the breaking stress increases with increasing degree of orientation as well (Fig. 10). The stress-orientation relation implies that more highly oriented crystallites become aligned more nearly parallel to the fiber axis, and hence are in a better position to support the load. Additionally, the crystallite size reaches its smallest value (Table 1) together with the maximum alignment that is attained at 10–20 mms^{-1}. A smaller crystallite size means a smaller number of defects in the crystallites, therefore the reduced size of the crystallites could be another contributor to the improvement of the breaking stress and the yield stress (Fig. 9).

On the other hand, the amorphous chains become extended and aligned in the direction of the fiber axis, together with aligned crystallites, when the reeling speed increases up to 10–20 mms^{-1} as illustrated in Fig. 7. Such an alignment of amorphous chains along the fiber may lead to a rise of the intercrystallite distance and a limit on the possible deformation of the silk when the silk comes under tensile tests. For that reason, the yield strain and breaking strain are smaller compared with the silk of which the amorphous chains are in a rather relaxed state at low reeling speed (Fig. 9). Thus the yield strain and breaking strain drop with increasing reeling speed until the maximum alignment of the crystallites and the amorphous chains reaches at 10–20 mms^{-1}.

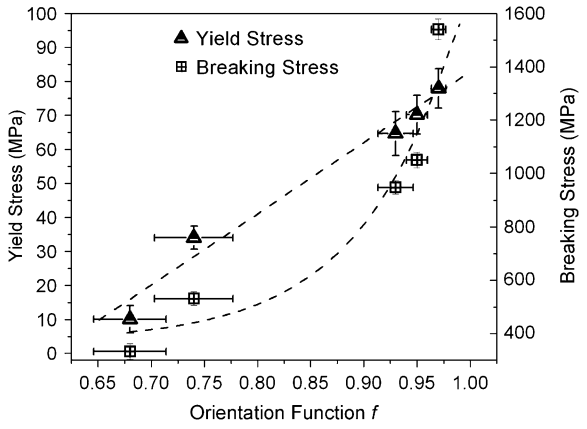

FIGURE 10 Relation between orientation function and stress of spider dragline silk.

CONCLUSIONS

Based on the result of WAXS and SAXS, and on AFM images, we propose what we believe is a new model to describe the hierarchical structure of silk. It is found that the protein polypeptide chain network structure of spider dragline silk changes substantially with reeling speed. This network structure to a large extent determines the mechanical properties. The crystallite size and orientation are important structural factors to decide the strength of silk. Enhancement of the silk strength can be achieved by decreasing crystallite size and increasing degree of orientation of crystallites. For spider dragline silk, the highest degree of orientation is almost reached at the natural reeling speed for spiders, and it remains as constant upon a further increase of the reeling speed. This may lead directly to the stable mechanical performance of spider silk exhibited in nature. It is hoped that this understanding will provide new insights on designing advanced synthetic materials through mimicking or improving the spider silk mechanical properties.

We are grateful to Mr. Poh Chong Lim for his technical assistance in WAXS measurement. We thank Dr. C. Strom for valuable suggestions and critical reading of the manuscript.

REFERENCES

1. Hinman, M. B., J. A. Jones, and R. V. Lewis. 2000. Synthetic spider silk: a modular fiber. *Trends Biotechnol.* 18:374–379.
2. Hayashi, C. Y., N. H. Shipley, and R. V. Lewis. 1999. Hypotheses that correlate the sequence, structure, and mechanical properties of spider silk proteins. *Int. J. Biol. Macromol.* 24:271–275.
3. Tirrell, D. A. 1996. Putting a new spin on spider silk. *Science.* 271: 39–40.
4. Cunniff, P. M., S. A. Fossey, M. A. Auerbach, J. W. Song, D. L. Kaplan, W. W. Adams, R. K. Eby, D. Mahoney, and D. L. Vezie. 1994. Mechanical and thermal properties of dragline silk from the spider *Nephila clavipes*. *Polym. Adv. Technol.* 5:401–410.
5. Vollrath, F. 2000. Strength and structure of spiders' silks. *Rev. Mol. Biotechnol.* 74:67–83.
6. Kaplan, D. L., W. W. Adams, C. Viney, and B. L. Farmer. 1994. Silk: biology, structure, properties, and genetics. *In* Silk Polymers-Material Science and Biotechnology, D. Kaplan, W. W. Adams, B. Farmer, and C. Viney, editors. American Chemical Society, Washington, DC. 2–16.
7. Xu, M., and R. V. Lewis. 1990. Structure of a protein superfiber: spider dragline silk. *Proc. Natl. Acad. Sci. USA.* 87:7120–7124.
8. Vollrath, F., and D. P. Knight. 2001. Liquid crystalline spinning of spider silk. *Nature.* 410:541–548.
9. Simmons, A., E. Ray, and L. W. Jelinski. 1994. Solid-state 13C NMR of *Nephila clavipes* dragline silk establishes structure and identity of crystalline regions. *Macromolecules.* 27:5235–5237.
10. Kummerlen, J., J. D. van Beek, F. Vollrath, and B. H. Meier. 1996. Local structure in spider dragline silk investigated by two-dimensional spin-diffusion nuclear magnetic resonance. *Macromolecules.* 29:2920–2928.
11. Warwicker, J. O. 1960. Comparative studies of fibrous. II. The crystal structure of various fibroins. *J. Mol. Biol.* 2:350–362.
12. Simmons, A. H., C. A. Michal, and L. W. Jelinski. 1996. Molecular orientation and two-component nature of the crystalline fraction of spider dragline silk. *Science.* 271:84–87.

13. Oroudjev, E., J. Soares, S. Arcidiacono, J. B. Thompson, S. A. Fossey, and H. G. Hansma. 2002. Segmented nanofibers of spider dragline silk: Atomic force microscopy and single-molecule force spectroscopy. *Proc. Natl. Acad. Sci. USA*. 99:6460–6465.

14. Calvert, P. 1998. Materials science: silk and sequence. *Nature*. 393: 309–311.

15. Vollrath, F., B. Madsen, and Z. Shao. 2001. The effect of spinning conditions on the mechanics of a spider's dragline silk. *Proc. R. Soc. Lond. B Biol. Sci.* 268:2339–2346.

16. Madsen, B., and F. Vollrath. 2000. Mechanics and morphology of silk reeled from anaesthetized spiders. *Naturwissenschaften*. 27:148–153.

17. Putthanarat, S., N. Stribeck, S. A. Fossey, R. K. Eby, and W. W. Adams. 2000. Investigation of nanofibrils of silk fibers. *Polym.* 41: 7735–7747.

18. Gould, S. A. C., K. T. Tran, J. C. Spagna, A. M. F. Moore, and J. B. Shulman. 1999. Short and long range order of the morphology of silk from *Latrodectus hesperus* (Black Widow) as characterized by atomic force microscope. *Int. J. Biol. Macromol.* 24:151–157.

19. Silva, D. 2004. Revision of the spider genus *Caloctenus* Keyserling, 1877 (*Araneae, Ctenidae*). Rev. Peru. Biol. 11:5–26.

20. Cullity, B. D. 1959. Chapter 3 Diffraction I: The directions of diffracted beams. *In* Elements of X-Ray Diffraction. B. D. Cullity, editor. Addison-Wesley, Waltham, MA. 99.

21. Grubb, D. T., and L. W. Jelinski. 1997. Fiber morphology of spider silk: the effect of tensile deformation. *Macromolecules*. 30:2860–2867.

22. Li, G., P. Zhou, Z. Shao, X. Xie, X. Chen, H. Wang, L. Chunyu, and T. Yu. 2001. The natural silk spinning process: a nucleation-dependent aggregation mechanism? *Eur. J. Biochem.* 268:6600–6606.

23. Vinney, C., A. E. Huber, D. L. Dunaway, K. Kerkam, and S. T. Case. 1993. Optical characterization of silk secretion and fibers. *In* Silk Fibers Material Science and Biotechnology. D. Kaplan, W. W. Adams, B. Farmer, and C. Viney, editors. ACS Symposium Series 544. 121–136.

24. Vollrath, F., and D. P. Knight. 2001. Liquid crystalline spinning of spider silk. *Nature*. 410:541–548.

25. Liu, X. Y. 2001. Generic mechanism of heterogeneous nucleation and molecular interfacial effect. *In* Advances in Crystal Growth Research. K. Sato, K. Nakajima, and Y. Furukawa, editors. Elsevier Science B.V., Amsterdam, The Netherlands. 42–61.

26. Denny, M. W. 1980. Silks—their properties and functions. *In* The Mechanical Properties of Biological Materials. C. J. F. V. Vincent, and J. D. Currey, editors. Cambridge University Press, Cambridge, UK. 247–272.

27. Riekel, C., B. Madsen, D. Knight, and F. Vollrath. 2000. X-ray diffraction on spider silk during controlled extrusion under a synchrotron radiation x-ray beam. *Biomacromolecules*. 1:622–626.

28. Miller, L. D., S. Putthanarat, R. K. Eby, and W. W. Adams. 1999. Investigation of the nanofibrillar morphology in silk fibers by small angle X-ray scattering and atomic microscope. *Int. J. Biol. Macromol.* 24:159–165.

29. Gupta, A. K. 1997. Characterization of polymers and fibres. *In* Manufactured Fiber Technology. V. B. Gupta and V. K. Kothari, editors. Chapman & Hall, London. 203–247.

30. Kanaya, T., M. Ohkura, and K. Kaji. 1994. Structure of poly(vinyl alcohol) gels studied by wide- and small-angle neutron scattering. *Macromolecules*. 27:5609–5615.

31. Kohler, T., and F. Vollrath. 1995. Thread biomechanics in the two orb-weaving spiders *Araneus diadematus* (*Araneae, Araneidae*) and *Uloborus walckenaerius* (*Araneae, Uloboridae*). *J. Exp. Zool.* 271:1–17.

32. Shao, Z., R. Young, and F. Vollrath. 1999. The effect of solvents on spider silk studied by mechanical testing and single-fibre Raman spectroscopy. *Int. J. Biol. Macromol.* 24:295–300.